Available online at www.sciencedirect.com

ScienceDirect

Chinese Journal of Aeronautics 21(2008) 207-214

Chinese Journal of Aeronautics

www.elsevier.com/locate/cja

A Ventral Diverterless High Offset S-shaped Inlet at Transonic Speeds

Xie Wenzhong*, Guo Rongwei

College of Energy and Power Engineering, Nanjing University of Aeronautics and Astronautics, Nanjing 210016, China

Received 13 September 2007; accepted 18 December 2007

Abstract

An investigation on the ventral diverterless high offset S-shaped inlet is carried out at Mach numbers from 0.600 to 1.534, angles of attack from –4º to 9.4º, and yaw angles from 0º to 8º. Results indicate: (1) a large region of low total pressure exists at the lower part of the inlet exit caused by the counter-rotating vortices in the S-shaped duct; (2) the performances of the inlet at Mach number 1.000 reach almost the highest, so the propulsion system could work efficiently in terms of aerodynamics; (3) the total pressure recovery increases slowly at first and then remains unvaried as the Mach number rises from 0.6 to 1.0, however, it does in an opposite manner in the conventional diverter-equipped S-shaped inlet; (4) the performances of the inlet are generally insensitive to angles of attack from –4º to 9.4º and yaw angles from 0º to 8º at Mach number 0.850, and angles of attack from –2º to 6º and yaw angles from 0º to 5º at Mach number 1.534.

Keywords: aerospace propulsion system; diverterless inlet; high offset; transonic inlet; S-shaped inlet; experimental investigation

1 Introduction

Out of the multi-purpose tactical missions, modern fighters always have to fly at transonic speeds, which poses a major technical challenge to the inlet designers that an excellent inlet/engine adaptability under wide flight conditions is urgently required taking into consideration the low radar cross section (RCS).

The diverterless supersonic inlet (DSI) of the Lockheed Martin joint strike fighter (JSF), which operates mostly at transonic speeds, has been designed taking whatever is mentioned above into enough account. Fundamental researches on this inlet configuration have been continued since the mid-1990s. A three-dimensional surface, or a bump, which functions as a compression surface and creates a pressure distribution that pushes boundary layer air away from the inlet, is formed on the surface of the fuselage in the aperture area. The inlet cowl lips are so designed as to allow most of boundary layer flow to spill out of the aft notch. The DSI structure complexity has been greatly reduced by the removal of moving parts, a boundary layer diverter and a bleed or bypass system thus decreasing the aircraft's empty weight, production cost, and requirements of maintenance-supporting equipment[1-2]. Furthermore, by eliminating the surface discontinuity of the diverter, the forward sweep cowl lips and the S-shaped duct, which houses the mental blades within the engine's compressor, the bump can decrease the RCS efficiently.

Recently lots of researchers have been working on the diverterless inlets. In Refs.[3-4], a design method of a top-mounted diverterless subsonic inlet was presented associated with a fuselage shape like

*Corresponding author. Tel.: +86-25-84892200-2415.
E-mail address: xie_wenzhong@126.com
Foundation item: National Basic Research Program of China (5130802)

the Global Hawk UAV. And the design method has been verified by numerical simulation and wind tunnel tests. But the speed range of the UAV in Refs.[3-4] is subsonic. In Ref.[5], the mechanism of the DSI for diverting the boundary layer with numerical simulation was analyzed. With help of different inlet configurations, Refs.[6-8] each developed DSI design methods, which have been validated too in experiments. In Ref.[9], experimental results revealed that the sub-critical margin of DSI is broader than that of the conventional supersonic inlet, and in Ref.[10], were experimentally investigated the effects of the entrance parameters of the DSI on the RCS.

However, so far the researches on diverterless inlets have only focused on the partial line-of-sight blockage into the engine. This means that the metal blades inside the engine's compressor directly reflect the radar energy over some viewing angles thereby increasing the RCS of the aircraft. A retrieval of publicized literature shows that there is hardly found any information about the bump inlet design with a duct to provide 100% line-of-sight blockage into the engine over all viewing angles. Refs.[11-13] pointed out that the inlet design with a duct like this could achieve low RCS. Therefore, it is worth while making further and deeper researches in this field.

This paper begins with an experimental study on the aerodynamic characteristics of a ventral diverterless high offset S-shaped inlet at transonic speeds, which is of 100% line-of-sight blockage into the engine face. From this study, the inlet performances are obtained at different angles of attack, yaw angles, free stream Mach numbers and mass flow coefficients. This paper also presents static pressure coefficient distribution along the walls and total pressure recovery contours at the engine face. The results show that the aerodynamic characteristics of the inlet are good enough to match the engine.

2 Test Model and Devices

Fig.1 gives the schematic view of the inlet model, which includes a forebody, an aperture, an S-shaped duct and a straight diffuser with the lengths specified in the figure. The offset of the S-shaped duct is 0.82D, where D is the diameter of the inlet's exit. This inlet design provides 100% line-of-sight blockage into the engine face. The sweep-forward angles of the lower lip and side lip are 30º and 47º respectively. The area ratio between the inlet exit and the throat (A_2/A_{th}) is 1.3.

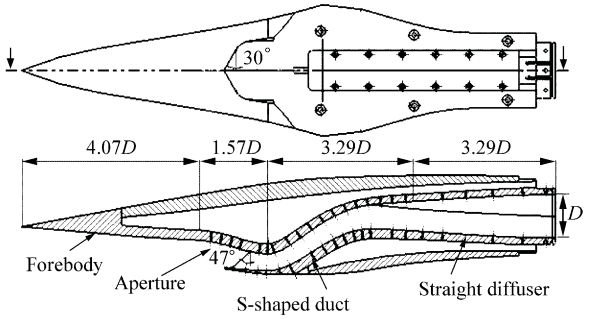

Fig.1 Schematic view of the inlet model.

In order to obtain the inlet pressure recovery, distortion parameters and mass flow, at the aerodynamic interface plane (AIP) are located a 40- probe total pressure rake with 8 arms (located 45° apart) and 5 instrumentation rings (5 probes with equal areas on each arm) and 8 static pressure orifices. For the purpose of analyzing the flow characteristics of the inlet, the model is provided with 42 static pressure orifices along the top wall (R1-R23) and the bottom wall (C1-C19) at symmetric section. The orifices R6 and C3 are located at the throat section. The mass flow plug, placed at the model exit and driven by an electric motor, provides flow control in measurements at different mass flow rates.

The tests were carried out in the NH-1 high speed wind tunnel at Nanjing University of Aeronautics and Astronautics. The test section is of a square 600 mm × 600 mm. The unit Reynolds number of the wind tunnel ranges from 1.20×10^7 to 1.77×10^7. During the tests, the free stream Mach number varies from 0.600 to 1.534, angles of attack from –4° to 9.4° and yaw angles from 0° to 8°. The blockage ratio of the inlet model to the wind tunnel is about 4.6%. Fig.2 shows the inlet model in wind tunnel.

Fig.2 Inlet model in wind tunnel.

3 Experimental Results and Discussions

The paper evaluates the performances of the inlet in terms of the total pressure recovery σ, the mass-flow coefficient ϕ and the circumferential total pressure distortion DC_{60} (which is compared with the absolute value) tested over a wide range of test conditions. The effects of mass flow ratio，free stream Mach number Ma_0, angle of attack α and yaw angle β on the performance of the inlet are obtained. It should be noted that the inlet's exit Mach number (Ma_2) of the design point is 0.45.

3.1 Static pressure coefficient distribution along the walls

Fig.3 exhibits the static pressure coefficient distribution along the walls at different free stream Mach numbers with angle of attack and yaw angle equal to zero. At the high subsonic speed Ma_0 = 0.850, the static pressure on the top surface in front of the aperture (R1-R3) rises because the mass flow coefficient is less than 1.00. From R4 to R7, the static pressure decreases due to the flow acceleration over the bump surface. On the bottom surface from C1 to C4, owing to the local diffusing stream tube caused by the concave surface, the static pressure increases. When the flow enters the S-shaped tube, the static pressure along the top and bottom walls distributes in a typical X-form manner. At the entrance of the S-shaped duct, the static pressure on the bottom surface is 0.45 higher than that on the top surface, which causes the boundary layer to move to the top surface. To the contrary, the static pressure on the top surface is about 0.36 higher than that on the bottom surface near the exit of the

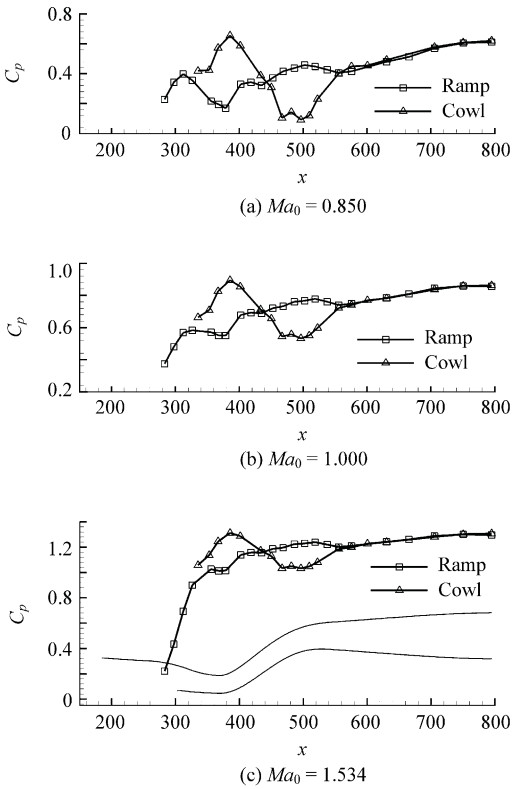

Fig.3 Static pressure coefficient distribution along the walls.

S-shaped duct, which causes the boundary layer to accumulate on the top surface. When the flow enters the straight diffuser, the static pressure difference between the top and the bottom surfaces declines to zero gradually, and, at the same time, the static pressure along walls increases slowly. At Mach number 1.000, the static pressure along the walls changes in the way similar to that at the high subsonic speeds. But the drops of the static pressure from R4 to R7 are smaller and its surges from C1 to C2 sharper than those at the high subsonic speeds. This can be attributed to the fact that because the mass flow coefficients of the inlet at Mach number 1.000 are lower than those at high subsonic speeds, the equivalent cone angle of the pre-entry stream tube at Mach number 1.000 is larger, which alleviates the flow expansion over the bump surface and strengthens its compression on the bottom concave surface. However, the fact that none of sudden static pressure rises take place within the flow path indicates the absence of strong compression such as shock waves. Different from the case of Mach

number 1.000, at the low supersonic speed Ma_0 = 1.534, the rise of the static pressure from R1 to R5 is much sharper, which is caused by the shock waves on the bump surface.

3.2 Total pressure recovery contours on the engine face

Fig.4 shows the total pressure distribution on the engine face while Ma_0 = 0.850, 1.000 and 1.534 when α = 0º and β = 0º. From the figure, significant pressure deficits could be observed at the bottom of the section of engine face at transonic speeds. Because of the thick boundary layer on the top surface in front of the entrance of the S-shaped duct and the long straight diffuser, the secondary flows on the engine face are expected to be dominated by the counter-rotating vortices formed at the second turn of the S-shaped duct[14-15], which pushes the boundary layer towards the bottom surface leading to appearance of the "pool" of lower total pressure on the engine face. Fig.4 also shows that the total pressure contours at Mach number 1.000 are very similar to those at high subsonic speeds except that the region of low total pressure at the bottom of the engine face is smaller. Besides, the total pressure contour at the low supersonic speed is lower than those at subsonic speed and Mach number 1.000, and the proportion of the high total pressure region looks obviously smaller.

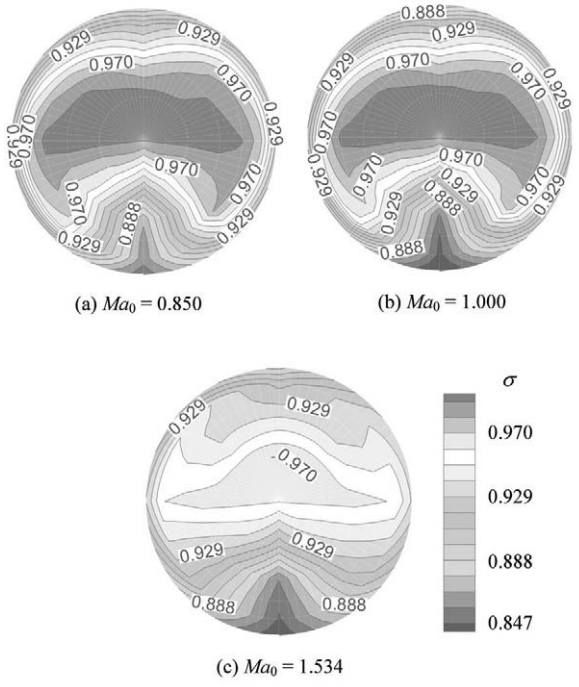

Fig.4 Total pressure recovery contours on the engine face.

3.3 Effects of mass flow coefficient

Fig.5 shows the effects of mass flow coefficient on the total pressure recovery, when Ma_0 = 0.850, 1.000 and 1.534 when α = 0º and β = 0º. The total pressure recovery decreases as the mass flow coefficient increases. With the designed mass flow coefficient, the total pressure recovery is 0.965 at Ma_0 = 0.850 and Ma_0 = 1.000, and 0.932 at Ma_0 = 1.534. The variation of the pressure recovery with the mass flow coefficient could be explained as follows: ① consequent on the removal of a diverter and the presence of a forward sweep lip, when the mass flow coefficient increases, the cross pressure gradient on the bump surface decreases, which increases the amount of boundary layer ingested into the inlet duct; ② the Mach number of the inlet duct increases as the mass flow coefficient rises thereby increasing the friction loss; ③ an additional pressure recovery penalty is generated by the critical shock waves happening somewhere in the duct, when the mass flow coefficient exceeds a certain value at Ma_0 = 1.000 and Ma_0 = 1.534 in particular.

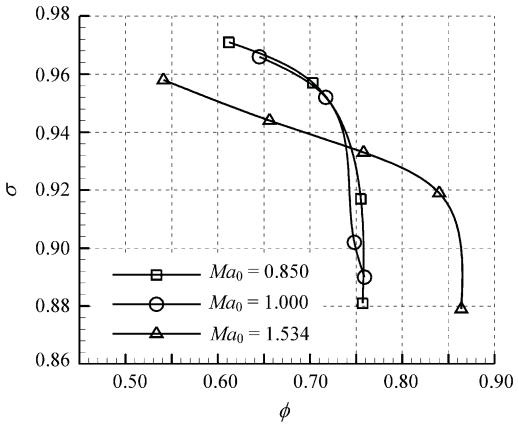

Fig.5 Total pressure recovery with mass-flow coefficient.

Fig.6 shows the effects of the mass flow coefficient on the distortion index DC_{60}. It could be seen that at Ma_0 = 0.850, the distortion index DC_{60} increases in absolute values with the mass flow coef-

ficient increasing, and the value amounts to –0.354 with the designed mass flow coefficient. Generally, this results from the increases of the amount of the boundary layer ingested into the duct with the increased mass flow coefficient and the dilation of the region of low total pressure at the bottom of the engine face. At $Ma_0 = 1.000$ and 1.534, the distortion index DC_{60} fluctuates as the mass flow coefficient varies, and the value is –0.329 and –0.431 respectively with the designed mass flow coefficient. This is probably attributable to the change of the moving path of the boundary layer caused by the critical shock waves happening somewhere in the inlet duct, when the mass flow coefficient exceeds a certain value.

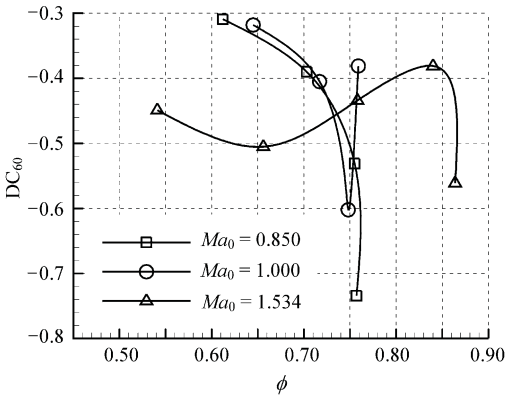

Fig.6 Distortion index DC_{60} with mass flow coefficient.

3.4 Effects of free stream Mach number

Fig.7 illustrates the effects of the free stream Mach number on the mass flow coefficient and total pressure recovery when $\alpha = 0°$ and $\beta = 0°$. As the free stream Mach number increases, the mass flow coefficient decreases, and, after reaching the minimum at Mach number 1.000, it increases. Fig.7 also shows that the total pressure rises and remains constant when the free stream Mach number is up from 0.600 to 1.000, and, afterwards, drops sharply while the free stream Mach number approaches the supersonic. In the conventional diverter-equipped S-shaped inlet, the total pressure recovery decreases slightly as the free stream Mach number increases within the range of subsonic speeds. In a diverterless inlet under discussion, however, the total pressure recovery appears disparate: the amount of the boundary layer ingested into the inlet duct is different with different mass flow coefficients caused by different free stream Mach numbers, and the friction loss of the flow path increases with the increased free steam Mach number. In addition, as the free stream Mach number exceeds 1.000, the total pressure loss will further increase owing to the disappearence of the shock wave and the shock-boundary layer interaction.

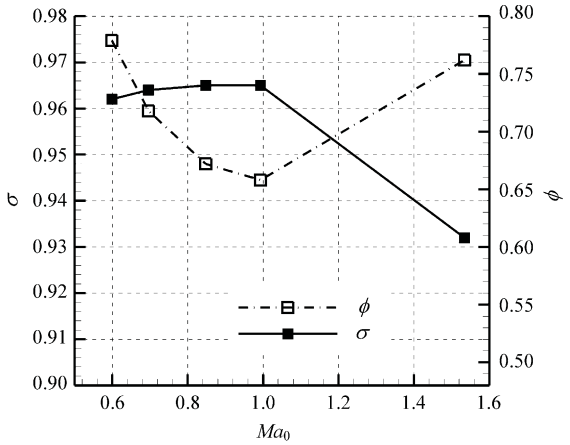

Fig.7 Mass flow coefficient and total pressure recovery vs free steam Mach number.

Fig.8 shows the effects of the free stream Mach number on the distortion index DC_{60} when $\alpha = 0°$ and $\beta = 0°$. As the free stream Mach number increases, the distortion index DC_{60} decreases, and, after reaching the minimum at Mach number 1.000, it increases. From Fig.8, it is seen that all the absolute values are below 0.5 during tests.

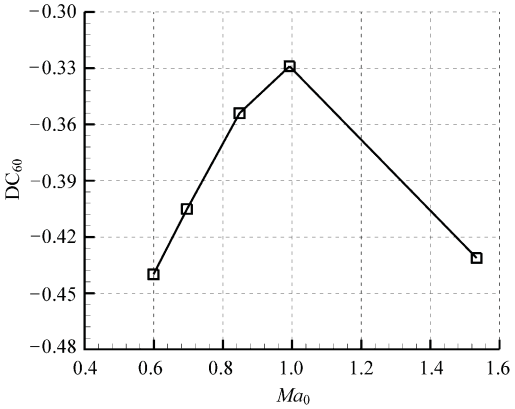

Fig.8 Distortion index DC_{60} vs free steam Mach number.

3.5 Effects of angle of attack

Fig.9 shows the effects of the angle of attack on the mass flow coefficient and the total pressure recovery with 0º yaw angle. It indicates very little effects that the angle of attack could produce on the mass flow coefficient and the total pressure recovery. The mass flow coefficient fluctuates 1.3% with the angle of attack from –4º to 9.4º at Ma_0 = 0.850, and 0.4% with the angle of attack from –2º to 6º at Ma_0= 1.534. The total pressure recovery fluctuates 0.6% with the angle of attack from –4º to 9.4º at Ma_0 = 0.850, and 0.1% with the angle of attack from –2º to 6º at Ma_0 = 1.534.

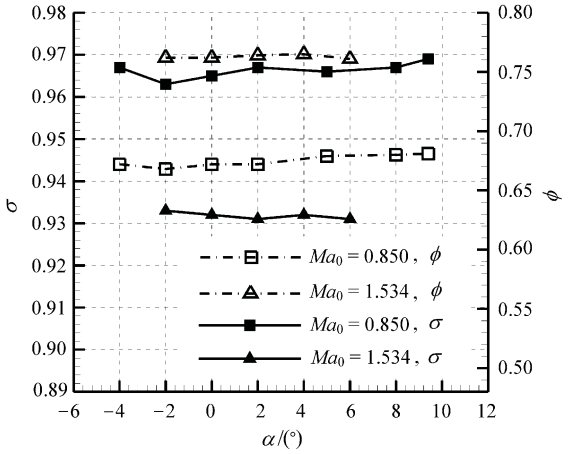

Fig.9 Effects of angle of attack on mass flow coefficient and total pressure recovery.

Fig.10 shows the variation of the distortion index DC_{60} against the angle of attack with 0º yaw angle at Ma_0 = 0.850 and 1.534. It can be observed that as the angle of attack increases from 0º, the distortion index decreases at both Ma_0. Nevertheless, when the angle of attack ranges between 4º and 6º at Ma_0 = 1.534, some drops could be found in the distortion index, but distortion at the angle of attack 6º is still lower than that at 0º incidence.

The performances of the inlet are generally insensitive to the angle of attack, and a little amelioration of flow distortion would result with the angle of attack deviating from 0º. This is mainly credited to the beneficial ventral configuration. Because of the shield of the forebody, the local angle of attack at the inlet entrance is smaller than that of free stream, and the flow separation on inner surface of the lip may not occur during the tests.

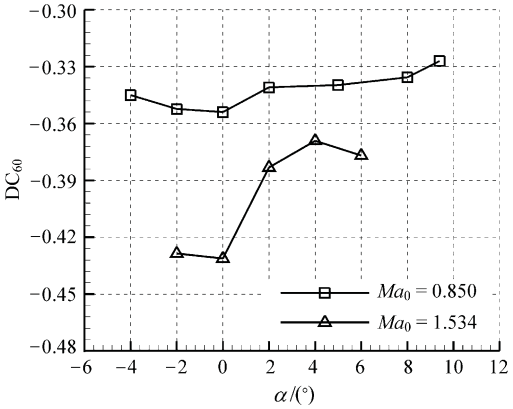

Fig.10 Effects of angle of attack on distortion index.

3.6 Effects of yaw angle

Fig.11 shows the effects of the yaw angle on the mass flow coefficient and the total pressure recovery at zero incidence. As the yaw angle increases, the mass flow coefficient changes very little within the range of 0.9% at Ma_0 = 0.850 and 0.3% at Ma_0 = 1.534, and the total pressure recovery decreases slightly by 0.5% as the yaw angle varies from 0º to 8º at Ma_0 = 0.850 and 0.4% from 0º to 5º at Ma_0 = 1.534.

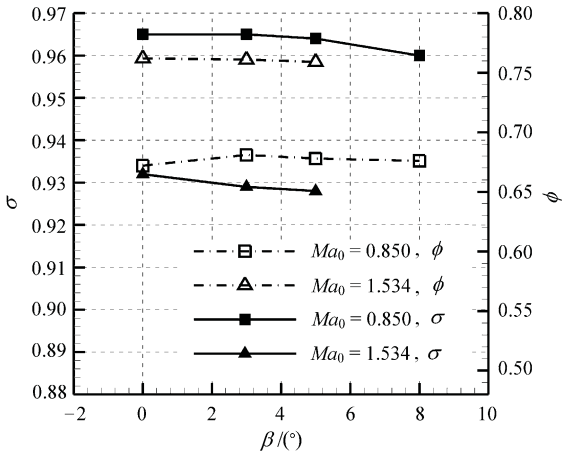

Fig.11 Mass flow coefficient and total pressure recovery vs yaw angle.

Fig.12 shows the variation of the distortion index as a function of the yaw angle. It shows that when Ma_0 = 0.850, as the yaw angle increases, the distortion index increases and then decreases; when

Ma_0 = 1.534, the distortion index decreases with the yaw angle increasing from 0º to 5º. It can be seen that the maximum absolute value of the distortion index DC_{60} is always lower than 0.5.

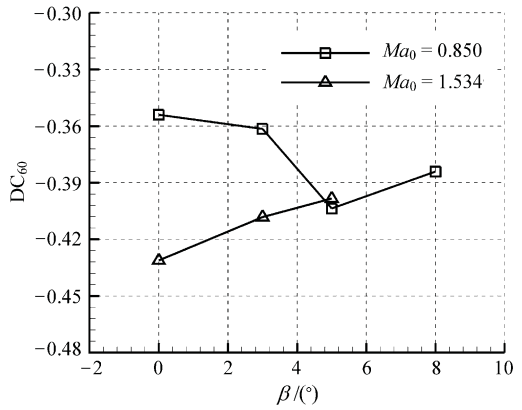

Fig.12 Distortion index DC_{60} vs yaw angle.

4 Conclusions

A wind-tunnel test of a ventral diverterless high offset S-shaped inlet has been carried out to investigate the aerodynamic characteristics at transonic speeds. Some conclusions can be drawn as follows:

(1) There is a large region of low total pressure at the lower part of the inlet exit caused by the counter-rotating vortices formed at the second turn of the S-shaped duct.

(2) The performances of the inlet reach almost the highest at Mach number 1.000. This renders the propulsion system able to work with high efficiency in terms of aerodynamics.

(3) As the mass flow coefficient increases, the total pressure recovery decreases; the distortion increases at Ma_0 = 0.850, but fluctuates at Ma_0 = 1.000 and 1.534.

(4) The total pressure recovery increases slowly first, and then remains unchanged as the Mach number rises from 0.600 to 1.000.

(5) The performances of the inlet are generally insensitive to angles of attack from –4º to 9.4º and yaw angles from 0º to 8º at Mach number 0.850, and angles of attack from –2º to 6º and yaw angles from 0º to 5º at Mach number 1.534.

References

[1] Hamstra J W, Mccallum B N, Sylvester T G, et al. Transition shoulder system and method for diverting boundary layer air. US Patent 005749542, 1998.

[2] Mcfarlan J D. Joint strike fighter diverterless supersonic inlet. US: National Press Club, 2000.

[3] Tan H J, Guo R W. Design and wind tunnel study of a top mounted diverterless inlet. Chinese Journal of Aeronautics 2004; 17(2): 72-78.

[4] Tan H J, Guo R W. Numerical simulation investigation and experimental validation of a top-mounted diverterless inlet and its validation. Acta Aeronautica et Astronautica Sinica 2004; 25(6): 540-545. [in Chinese]

[5] Liang D W, Li B. Reverse design of diverterless inlet and mechanism of diversion of boundary layer. Acta Aeronautica et Astronautica Sinica 2005; 26(3): 286-289. [in Chinese]

[6] Yang Y K. Design of bump inlet of thunder/JF-17 aircraft. Journal of Nanjing University of Aeronautics and Astronautics 2007; 39(4): 449-452. [in Chinese]

[7] Zhong Y C, Yu S Z, Wu Q. Research of bump inlet (DSI) model design and its aerodynamic propertiesp. Journal of Aerospace Power 2005; 20(5): 740-745. [in Chinese]

[8] Yin F, Wang J Q, Qiao S D. Study on the design of diverterless supersonic inlet. Aircraft Engineering 2006; (1): 25-27. [in Chinese]

[9] Ma X G. Study of buzz characteristics of the bump inlet. Aerodynamic Research and Experiment 2005; 22(1): 25-29. [in Chinese]

[10] Xie X M, Guo R W. Experimental research on RCS of bump inlet 2006; 27(2): 193-197. [in Chinese]

[11] Mayer D W, Bernhard H, Anderson T A J. 3D subsonic diffuser design and analysis. AIAA-98-3418, 1998.

[12] Sun S, Guo R W. Serpentine inlet performance enhancement using vortex generator based flow control. Chinese Journal of Aeronautics 2006; 19(1): 10-17.

[13] Shi L, Guo R W. A study of the electromagnetic scattering of a serpentine inlet. Acta Aeronautica et Astronautica Sinica 2007; 28(6): 1296-1301. [in Chinese]

[14] Seddon J, Goldsmith L. Intake aerodynamics. London: Blackwell Science Ltd, 1999: 338-340.

[15] Guo R W, Seddon J. Swirl characteristics of an S-shaped air intake with both horizontal and vertical offset. Aeronautical Quarterly 1983; 34: 130-146.

[16] Li Q T, Guo R W. Design and performance of S-shaped inlet for

high subsonic missile. Journal of Nanjing University of Aeronautics and Astronautics 2002; 34(2): 98-113. [in Chinese]

[17] Wan D W, Guo R W. Design and experimental study of an S-shaped inlet. Journal of Nanjing University of Aeronautics and Astronautics 2004; 36(2):150-154. [in Chinese]

[18] Xie L R, Guo R W. Design and experimental study of an S-shaped inlet restricted by missile[J]. Acta Aerodynamica Sinica 2006; 24(1): 95-101. [in Chinese]

Biography:

Xie Wenzhong Born in 1981, now he is a Ph.D. candidate in Nanjing University of Aeronautics and Astronautics. His academic interests are focused on CFD and experimenta1 investigation of internal flow.

E-mai1: xie_wenzhong@126.com